

## CHAPTER 8

### EMD CORRECTION OF ORBITAL DRIFT ARTIFACTS IN SATELLITE DATA STREAM

Jorge E. Pinzón, Molly E. Brown and Compton J. Tucker

Orbital drift results in late equatorial crossing times for the afternoon National Oceanic and Atmospheric Administration (NOAA) polar satellites and in changes of illumination that affect measurements made by the advanced very high resolution radiometer (AVHRR). Processing and correcting for calibration variation(s) and atmospheric effects have improved, but one of the standard AVHRR products, the normalized difference vegetation index (*NDVI*), may still contain variations due to orbital drift or changes in sun-target-sensor geometry. In this study, the solar zenith angle (SZA) trends associated with orbital drift are identified and analyzed with respect to their effects on the *NDVI*. The adaptive empirical mode decomposition (EMD) method is used to identify and remove the induced artifacts from the *NDVI* time series. The EMD is based on the local characteristic time scale of the data and is used to identify embedded nonlinear and nonstationary variation. Trend artifacts associated with drift were uncoupled from the surface signal, and their contributions were quantified at all latitudes. The approach was tested on 1 degree and 8-km *NDVI* global datasets, and showed that it is very suitable for addressing the long-standing issues of orbital shifting or the inconsistencies of the AVHRR data among sensors. The results showed that the interference of satellite drift artifacts with the surface signal was (i) large in a tropical forest, (ii) moderate in the tropics for less-densely vegetated areas, and (iii) lowest at higher northern and lower southern latitudes.

#### 8.1. Introduction

The use of the advanced very high resolution radiometer (AVHRR) data provided by the National Oceanic and Atmospheric Administration (NOAA) polar satellite series has demonstrated the potential of remote sensing for monitoring land-surface variables at a regional to a global scale. This archive of global 4-km AVHRR data was compiled from five different AVHRR instruments on five different NOAA polar-orbiting meteorological satellites (Cracknell 1997). Although recent sensors provide improved coarse resolution global land satellite data, the longest AVHRR record, which now extends over more than 23 years, constitutes an invaluable and irreplaceable archive of historical land information (Cracknell 1997, 2001).

Spectral vegetation indices are by far the most used of any of the products derived from the AVHRR instruments (Cracknell 2001, Los 1998, Tucker 1996), a development not anticipated by their designers (Cracknell 2001). These indices are

composed of red and near infrared radiances or reflectance, sometimes with additional channels included (Tucker 1979). For the AVHRR instruments, only two bands can be used. Consequently, most of these applications are based on the normalized difference vegetation index (*NDVI*), which is the ratio of the near infrared (NIR) and the red visible (VIS) radiances ,

$$NDVI = \frac{NIR - VIS}{NIR + VIS}. \quad (8.1)$$

This ratio yields a measure of photosynthetic capacity such that the higher the value of the ratio, the more photosynthetically active the cover type (Sellers 1985). Thus, the *NDVI* product provides the longest existing record of spatial coverage needed for monitoring global vegetation dynamics .

However, collecting a consistent time series record and linking historical observations to current and future measurements is a difficult task. Known inaccuracies for AVHRR arise from orbital drifts,<sup>††</sup> coarse resolution, lack of on-board calibration capability for the visible and near infrared channels, and their wide spectral bandwidths. These effects increase the probability of sub-pixel clouds that interfere with the surface signal, and increase the variation in the sun-target-view geometries convolved with surface bidirectional reflectance properties of the land surface, topography, and soil background reflectance (Privette et al. 1995). Overall, these inaccuracies result in both gradual and abrupt changes (artifacts) in the data with each successive satellite.

In order to reduce these inaccuracies, vicarious calibration, atmospheric correction and compositing techniques are commonly included in all *NDVI*-processing systems (Cihlar 1994, Los et al. 1994, Los 1998). Among these techniques, the maximum *NDVI* compositing technique has been used in nearly all operational AVHRR processing chains (Cracknell 2001). This procedure requires the processing of a series of multitemporal georeferenced satellite data into *NDVI* images. On a pixel-by-pixel basis, each *NDVI* value is examined, and only the highest value is retained for each pixel location. Holben (1986) showed that maximum *NDVI* imagery is highly related to green vegetation dynamics, and the aforementioned problems have been minimized. Moreover, Pinzón et al. (2001) showed that of the most commonly used compositing technique, the maximum *NDVI* provides an image with the highest spatial coherence.

The combined techniques used in most *NDVI* processing systems, although effective in reducing atmospheric and sun-target-sensor effects, which tend to cancel each other out (Holben 1986), are still confounded by variations of sun-target-sensor geometry and cloud contamination in some regions (Cihlar et al. 1998, Gutman 1999, Privette et al. 1995). Removing these artifacts from the *NDVI* time series remains a challenge, since an analytical or numerical solution to the system would

---

<sup>††</sup>The afternoon (PM) platforms drift about 20 to 40 minutes per year at later times of the day with a discontinuity drop back to earlier times of the day when the satellite changes (Price 1991, Los 1998).

be prohibitive with current real time processing, given the huge amount of data to process both spatially and temporally. Recent advances in atmospheric correction (El Saleous et al. 2000), bidirectional reflectance distribution functions (BRDF) (Schaaf 2002), and new capabilities for calibration as a result of crossovers with other satellites carrying more recent sensors have opened the way for significant improvements in data processing for the AVHRR sensor (El Saleous et al. 2000). However, this series of improvements has yet to be applied to the full AVHRR record and validated. Meanwhile, the *NDVI* may still contain variations due to orbital drift and changes in sun-target-sensor geometry, since the closure of such a system involves more unknowns than the measurable quantities (Myneni et al. 1993, Privette et al. 1995, Sellers et al. 1994).

Parametric approaches from model simulations to curve fitting have been used in the past, with a heavy set of simplifying assumptions (Gutman 1999, Los et al. 1994, Privette et al. 1995, Sellers et al. 1994). One main assumption is that any spurious trend in the *NDVI* over stable targets, e.g., deserts, can be linearly extrapolated and corrected in all surfaces. However, the complex interaction between vegetation responses, land cover, cloud contamination, bidirectional reflectance properties, and other *NDVI* dependencies prevent this generalization. Here, one can turn to the problem of inferring the underlying governing equations from measured data, or of the so-called observational approach (Gershfeld 1999). The empirical mode decomposition (EMD) is proposed as a means of separating the *NDVI* signal into components and identifying those that interfere with the surface signal, thus producing a consistent long record of remote sensing data for climate and vegetation studies. The EMD is based on the local characteristic time scale of the data and provides sharp identifications of embedded structures of nonlinear and nonstationary processes [see next section and, for more detail, Huang et al. (1998) for definitions]. To be precise, the *NDVI* and SZA signals are decomposed in terms of intrinsic mode functions (IMFs) by using the EMD to simplify and describe accurately the *NDVI*-SZA relationship. That is, one can tune the EMD to uncouple the seasonal and interannual components of the *NDVI* signals from SZA-drift induced structures.

This chapter is organized as follows. The standard processing of *NDVI* imagery is briefly described; this application of the EMD technique is presented with examples of trend detection in SZA latitudinal profiles to measure and correct orbital drift impact; a correction approach is tested and evaluated within the framework of EMD-filtering on 1 degree *NDVI* datasets; and finally, the extension to 8-km datasets is investigated, and the necessary pre-processing steps are described.

## 8.2. Processing of *NDVI* imagery

The *NDVI* data used in the analysis were the standard 8-km bimonthly continental maximum *NDVI* product of the Global Inventory Mapping and Monitoring System (GIMMS) group, from 1981 to the present (hereafter referred to as “the GIMMS

dataset”). This dataset was mapped to an Albers equal-area projection, calibrated by using the method of Vermote and Kaufman (1995) and corrected for sensor degradation by using a technique based on stable desert targets (Los 1998). The dataset also includes corrections for stratospheric volcanic aerosols for the April 1982 El Chichon eruption (applied to the data from April 1982 to December 1984) and the June 1991 Mt. Pinatubo eruption (applied to the data from June 1991 to December 1993). The technique uses maximum *NDVI* as a compositing technique with cloud screening based on an AVHRR channel 5 thermal threshold value over Africa (283K) and South America (273K). Pixels having scan angles greater than 45 degrees from nadir view and pixels associated with unrealistic reflectance values were also screened prior to compositing (see Mahoney et al. 2001 for more details of the GIMMS processing system).

The reliability of a long *NDVI* time series can be checked by examining the trends over regions of known and unchanging vegetation cover, such as deserts. From the other sources of *NDVI* variation other than land-surface vegetation, the solar zenith angle and, possibly, volcanic aerosols are known to cause a systematic trend in satellite datasets (Cihlar et al. 1998, Gutman 1999, Kaufmann et al. 2000). Independently, Los (1998), Kaufmann et al. (2000), and Slayback et al. (2003) showed that the effects of the solar zenith angle and volcanic aerosol on the *NDVI* over desert regions are negligible. Because these factors are small, residual errors in calibration are best detected from the desert *NDVI*. Three features of these desert time series are useful for evaluation: long-term trends, features at satellite transitions, and the variance. Slayback et al. (2003) reported that no trends, either for individual satellites or across the entire time period, were significant at the 95 percent level for different desert areas in the GIMMS dataset. However, Slayback et al. (2003) found statistically significant low-latitude trends from the 5° to 25° latitude bands, which are contaminated by substantial solar zenith angle effects and do not reflect real vegetative trends. Importantly, these researchers also reported that smooth trends were generally maintained across satellite transitions in desert signals, indicating the success of the calibration and sensor degradation schemes in intercalibrating the data from the various satellites to compose the GIMMS dataset (Slayback et al. 2003).

Figure 8.1 shows 1° × 1° uncorrected *NDVI* data at various latitude and longitude coordinates. Vegetated tropical areas (Fig. 8.1b–f), and especially tropical forests (Fig. 8.1c–f), present an evident trend connected to the orbital drift or SZA variation. Desert areas (Fig. 8.1a) and northern latitudes (Fig. 8.1g–i) appear less affected by changes in SZA due to orbital drift. These results are consistent with Slayback et al.’s (2003) observations. Previous studies of growing season patterns in northern latitudes (greater than 45°N) by using the *NDVI* from the AVHRR (Kaufmann et al. 2000, Myneni et al. 1997, Slayback et al. 2003, Tucker et al. 2001) found no statistically meaningful relation between *NDVI* trends and trends connected with the orbital drift or SZA variation. Qualitatively, this finding suggests

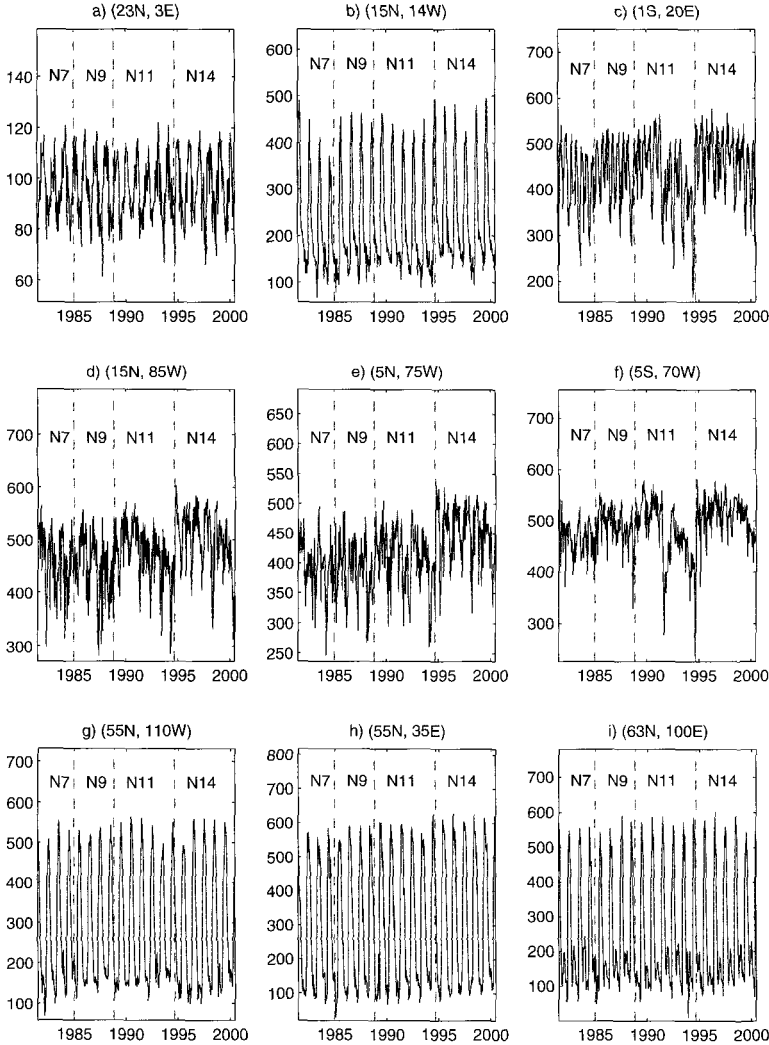


**Figure 8.1:** The  $1^\circ \times 1^\circ$  uncorrected  $NDVI \times 1000$  data at nine different locations. Note that the vertical scales are a function of land cover: vegetated tropical areas (b-f), and especially tropical forests (c-f), present an evident trend connected to the SZA variation; desert areas (a), and northern latitudes (g-i) appear less affected by changes in SZA.

that the magnitude of SZA trends at those higher latitudes is very small compared with the high seasonal variation in the  $NDVI$  of vegetated areas. Thus, the orbital drift's contribution would be minimal to the  $NDVI$  signal at those latitudes. However, explicit quantification of these contributions has not been reported. Moreover, Gutman (1999), using a different AVHRR dataset, doubted the reliability of  $NDVI$  data for inferring the northern latitude greening trend since potential artifacts related to SZA and intersensor changes could remain in the data. In the next section,

it is explained how to extract interannual trends from the *NDVI* signal, measure the contributions and significance of the *SZA* trends in the *NDVI* variability at all latitudes, and remove them from the *NDVI* signal accordingly.

### 8.3. Empirical mode decomposition

Huang et al. (1998) introduced empirical mode decomposition (EMD) as method for the representation of nonlinear and nonstationary data that shows clearly a physical scale or frequency content. As Huang et al. (1998, 1999) explained, the EMD method, contrary to almost all others previously proposed, is empirical, intuitive, direct, *a posteriori*, and adaptive, with the basis functions based on, and derived from, the data in question.

The decomposition uses the simple assumption that any data consist of different simple intrinsic modes of oscillations. Each mode may or may not be linear and will have the same number of extrema and zero-crossings. Furthermore, the oscillation will also be symmetric with respect to the “local mean.” At any given time, the data  $X(t)$  may have many different coexisting modes of oscillation, each one superimposed on the others. The result of combining these modes is the final complicated data. In the EMD, each of these oscillatory modes is represented by an intrinsic mode function (IMF) with the following definition: (a) in the whole dataset, the number of extrema and the number of zero-crossings must either be equal or differ at most by one, and (b) at any point, the mean value defined by the envelopes of local maxima and local minima is zero.

With this definition, one can decompose any function or data as follows: derive the “local mean”  $m_1$  by computing the mean between the upper envelope and lower envelope of the signal. The upper (lower) envelope is found by connecting all the local maxima (minima) by a cubic spline line. The difference,  $h_1 = X(t) - m_1$ , ideally should be an IMF, for the construction of  $h_1$  described above should satisfy all the requirements of an IMF. However, even if the fitting is perfect, a gentle hump on a slope can be amplified to become a local extremum, and a new iteration over  $h_1$  will be needed.

While the first condition is absolutely necessary for separating the intrinsic modes and for defining a meaningful instantaneous frequency, the second condition is also necessary in case the neighboring wave amplitudes have too large a disparity. In this way, one can actually recover the proper modes lost in an initial examination. Huang et al. (1998) named this process “sifting.” In fact, the sifting process can recover signals representing low amplitude riding waves by iteration. The procedure is illustrated in Huang et al. (1998,1999). The sifting process serves two purposes: to eliminate riding waves and to make the wave profiles more symmetric. Toward these ends, the sifting process has to be repeated as many times as are required to reduce the extracted signal to an IMF. In the subsequent sifting process,  $h_1$  is treated as the data, then  $h_1 - m_{11} = h_{11}$ . After repeated sifting, up to  $k$  times,  $h_{1k}$  becomes an IMF,  $h_{1(k-1)} - m_{1k} = h_{1k}$ ; then, the first IMF component

from the data is designated as  $c_1 = h_{1k}$ .

Overall,  $c_1$  should contain the finest scale or the shortest period component of the signal. We can separate  $c_1$  from the rest of the data by

$$X(t) - c_1 = r_1. \quad (8.2)$$

Since the residue  $r_1$  may still contain longer period components, it is treated as the new data and subjected to the same sifting process as described above. This procedure can be repeated to all the subsequent  $r_j$ 's, and the result is

$$r_1 - c_2 = r_2, \dots, r_{n-1} - c_n = r_n. \quad (8.3)$$

The sifting process can be stopped by any of the following predetermined criteria: either when the component  $c_n$  or the residue  $r_n$  becomes so small that it is less than the predetermined value of substantial consequence, or when the residue  $r_n$  becomes a monotonic function from which no more IMFs can be extracted. Even for data with zero mean, the final residue still can be different from zero. If the data have a trend, the final residue should be that trend. By summing up Eqs. (8.2) and (8.3), we finally obtain

$$X(t) = \sum_{j=1}^n c_j + r_n. \quad (8.4)$$

Thus, we achieve a decomposition of the data into  $n$ -implicit modes, with a residue  $r_n$ , which can be either the mean trend or a constant. The trends are obtained from the last IMFs of the EMD approach. In this application of the EMD, the SZA and NDVI signals are overextended at the boundaries with seasonal profiles with no trends to reduce known boundary problems in the EMD decomposition that might also affect the correction.

#### 8.4. Impact of orbital drift on NDVI and EMD-SZA filtering

This section presents EMD as a viable alternative to minimize NDVI SZA-inaccuracies and to characterize uncertainties more robustly than was possible previously. As discussed, the EMD method adjusts itself to local extrema and generates, by the sifting process, zero references and trends. Figure 8.2 shows the effects of the satellite drift on the SZA at different  $10^\circ$  latitude bands. An increasing trend is observed in each satellite due to its delay in the equatorial crossing time. This trend, superimposed on each plot, is accurately extracted and associated with the  $r_n$  component in the EMD iteration. The drift effects are more pronounced at lower latitudes (higher slopes), whereas seasonal variations dominate at higher latitudes in the two hemispheres. Note also that equatorial SZA plots ( $10^\circ\text{S}$  to  $10^\circ\text{N}$ ) have an extra oscillation due to the solar nadir moving past the target latitude, causing an increase in the SZA at six-month intervals rather than at yearly intervals (Privette et al. 1995).

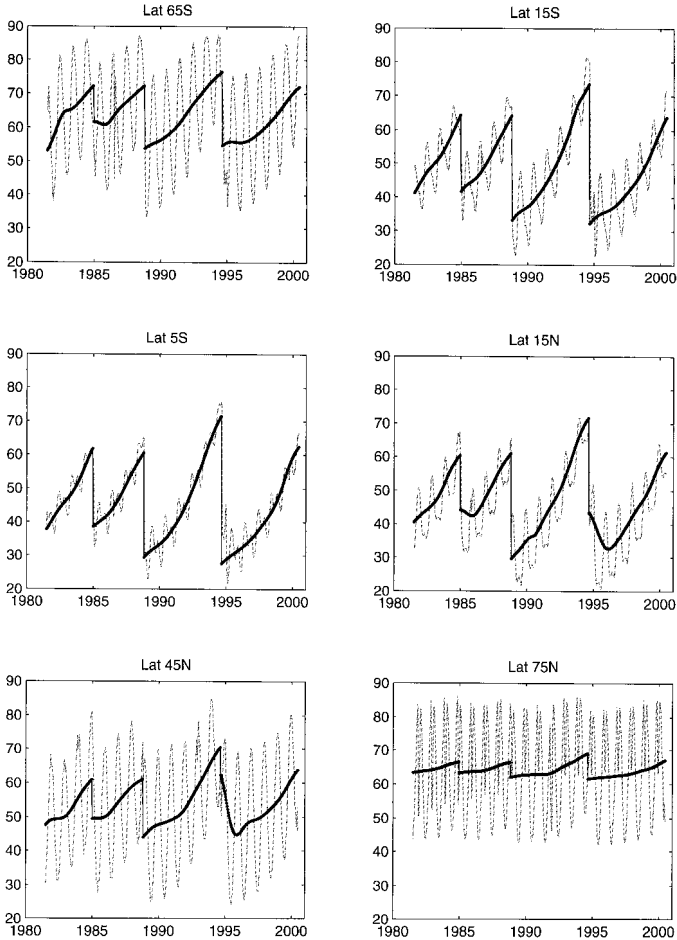


**Figure 8.2:** Solar zenith angle drift by  $10^\circ$  latitude bands. Drifts effects are more pronounced at lower latitudes (higher slopes), whereas seasonal variations dominate at higher latitudes in the two hemispheres. An extra oscillation is observed in equatorial plots ( $10^\circ\text{S}$  to  $10^\circ\text{N}$ ) due to the solar nadir moving past the target latitude. A remarkable extra oscillation in the  $60^\circ$ – $75^\circ\text{N}$  bin is observed. This oscillation is an indication of the data screening scheme used in the GIMMS dataset for very high solar zenith angles.

Similarly, the EMD is used to extract the *NDVI* trends that may be associated with satellite orbital drift, reducing the interference of many other components with the surface signal, for example.

The SZA values in general are different in the same latitudinal bins in the two hemispheres because of the difference in the local time of observation within the same orbit; i.e., on a given day, a given southern latitude is observed at a later local time than the same northern latitude. A remarkable extra oscillation is observed in the  $60^\circ$ – $75^\circ\text{N}$  bin. This oscillation is an indication of the data-screening scheme used in the GIMMS dataset for high SZA angles. Furthermore, this oscillation is an

artifact from the averaging over a wide range of latitudes when the SZA is greater than  $85^\circ$  during the winter and is reporting an arbitrary missing value. In the *NDVI* data, this artifact will be associated with terminator effects and screened out. As expected, this artifact is not observed in the highest southern bin since land-vegetation data goes only from  $40^\circ\text{S}$  to  $57^\circ\text{S}$ , and the SZA angles are less than  $85^\circ$  during the winter. The components of the EMD, as Fig. 8.2 suggests, are usually physically meaningful, since each scale is defined by the physical data themselves.

Similarly, the EMD is used to extract *NDVI* trends that may be associated with satellite orbital drift, reducing the interference of many other components with the surface signal, e.g., the BRDF, or the cloud contamination. Thus, *NDVI* time series are decomposed into two components for each satellite: a wave-seasonal and trend components. The hypothesis in this work is that if the *NDVI* is affected by orbital drift, its trend component is the one that should show this effect. Correlating the *NDVI*-trend and SZA-trend components, we can account for a large percentage ( $> 90\%$ ) of the solar zenith angle affect upon the *NDVI* (hereafter referred to as  $t_{szac}$ ), remove these effects from the *NDVI* data, leaving intact the phenologic components in the wave-seasonal components, and reconstruct the *NDVI* signal without the solar zenith angle variation.

In fact, as Huang et al. (1998) suggested, we can also use the IMF components as time-space filters. Traditionally, filtering is carried out in frequency space only. Using IMF, however, we can devise a time-space filtering. For example, the result of low, high, and band time-space EMD-filters in a signal having  $n$ -IMF components can be simply expressed as

$$X_{lk}(t) = \sum_{j=k_1}^n c_j + r_n,$$

$$X_{hk}(t) = \sum_{j=1}^{k_2} c_j, \quad (8.5)$$

and

$$X_{bk}(t) = \sum_{j=k_1}^{k_2} c_j,$$

respectively, where  $1 < k_1 < k_2 < n$ . The advantage of this time-space filtering is that the results preserve full meaning, nonlinearity and nonstationarity in physical space. The EMD-filtering strategy just described is summarized in Fig. 8.3.

To quantify more precisely the contribution of drift interference with the surface signals and their spatial distribution, a canonical correlation analysis was performed. This analysis is a multivariate statistical technique used to examine and describe the strength of a linear association between two sets of random variables (Bretherton et al. 1992, Cherry 1996, Wallace et al. 1992). The canonical correlation

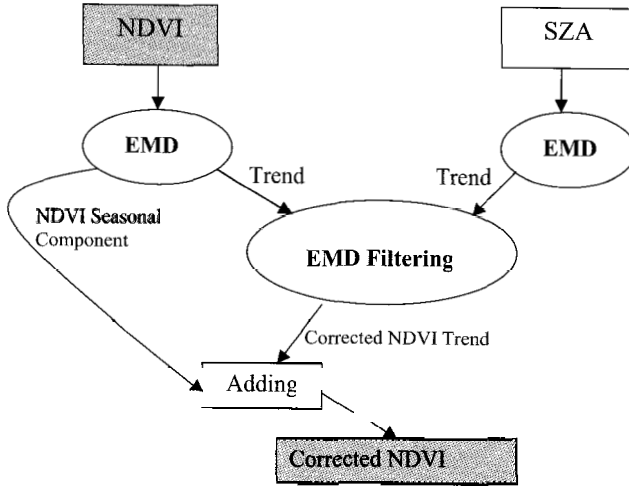


**Figure 8.3:** Flowchart of the solar zenith angle time-space EMD-filtering.

analysis is based on the singular value decomposition (SVD) of the paired-mode of the correlation matrix between the EMD-trend components of the *NDVI* and the *SZA*:  $[U, S, V] = \text{SVD}(A)$ , where  $A$  is the correlation matrix. The singular value decomposition of a matrix  $A$  produces a diagonal matrix  $S$  and a set of matrices  $U$ , and  $V$ , with orthonormal column vectors, such that  $A = U \times S \times V^t$ . The column vectors of the matrices  $U$  and  $V$ , referred to as the canonical factors, constitute an optimal orthonormal basis for the EMD-trend components of the *NDVI* and the *SZA*, respectively. The contribution of each canonical factor to the correlation matrix  $A$  is a function of the values in the diagonal matrix  $S$ , which are sorted in descending order. For more details about the singular value decomposition, see Golub and Van Loan (1989) and Trefethen and Bau (1997).

## 8.5. Results and discussion

In this section, we focus our EMD analysis on the global  $1^\circ$  degree *NDVI* time series starting in July 1981 (NOAA-7) and ending in November 2000 (NOAA-14). Table 8.1 shows the results of the *SZA* EMD-filtering approach for selected  $1^\circ$  latitude-longitude pixels from regions representing different biomes. It was found that the percentage variance of the *NDVI* variability explained by the filtered  $t_{szac}$  component decreased as the latitude increased (k-p) and as vegetation biomass decreased (a,b). This finding implies that  $t_{szac}$  variability is very small at those northern latitude regions and that the *NDVI* is minimally sensitive as the vegetation biomass decreases. This result is confirmed by the coefficient of determination between  $t_{szac}$  and the correspondent  $10^\circ$  latitude *SZA* trends. In most of those regions,  $r^2$  is less than 75, but not in tropical areas (c-h), especially tropical forests (c-g),

**Table 8.1:** Percentage variance of  $NDVI$  explained by the filtered  $t_{szac}$  component, coefficient of determination of orbital drift SZA trends and extracted  $NDVI$   $t_{szac}$ , and coefficient of determination of extracted  $t_{szac}$  and other  $NDVI$  trends: UNDMI (uncorrected), CNDMI (corrected). All coefficients are significant with  $p < 0.00001$ . Column (a) gives SZA and  $t_{szac}$ , column (b) reports the  $t_{szac}$  and UNDMI, and column (c) states the  $t_{szac}$  and CNDMI, respectively.

Location	(Lat, Lon)	%	$r^2 \times 100$		
			(a)	(b)	(c)
a) Sahara	(23°N, 3°E)	2	72	88	37
b) Sahel	(15°N, 14°W)	3	84	100	25
c) Central Forest	(1°S, 20°E)	14	87	100	27
d) Upper Guinea	(8°N, 5°W)	10	79	99	7
e) Center America	(15°N, 85°W)	18	86	99	27
f) Colombia	(5°N, 75°W)	29	89	99	25
g) Amazon	(5°S, 70°W)	23	87	100	37
h) NE-Brasil	(5°S, 38°W)	11	86	99	36
i) Indochina	(15°S, 105°E)	9	74	99	12
j) Australia	(25°S, 135°E)	26	92	91	56
k) Mexico	(27°N, 105°W)	8	71	83	26
l) Great plains	(45°N, 105°W)	2	80	97	37
m) Canada	(55°N, 110°W)	1	68	95	77
n) Labrador	(55°N, 65°W)	1	52	94	43
o) Central Russia	(55°N, 35°E)	1	68	96	60
p) Siberia	(63°N, 100°E)	1	51	98	58

where the percentage variance explained is greater than 10 and the  $r^2$  above 85. The coefficient of determination between  $t_{szac}$  and the uncorrected (UNDMI) and corrected (CNDMI) trends indicates that the EMD-filtering efficiently removed those artifacts related to the solar zenith angle and intersensor changes at all latitudes and biomes.

Each panel of Fig. 8.4 shows the uncorrected  $NDVI$  and its associated trend (U-time series), the solar zenith angle component  $t_{szac}$  removed (S in the figure) and the corresponding corrected  $NDVI$  and trend (C-time series), respectively. Each panel represents the same one degree time series at the latitude-longitude pixels described in Table 8.1. This figure confirms the main conclusion of Table 8.1: (1) regions in the tropics, especially tropical forests, are the most SZA-affected; (2) regions with a low vegetation biomass and at the high northern or low southern latitudes are least contaminated; and (3) all remaining components in the C-time series are found to be statistically independent of the SZA. Therefore, the EMD-filtering approach presented here constituted a sound SZA correction technique, especially in tropical

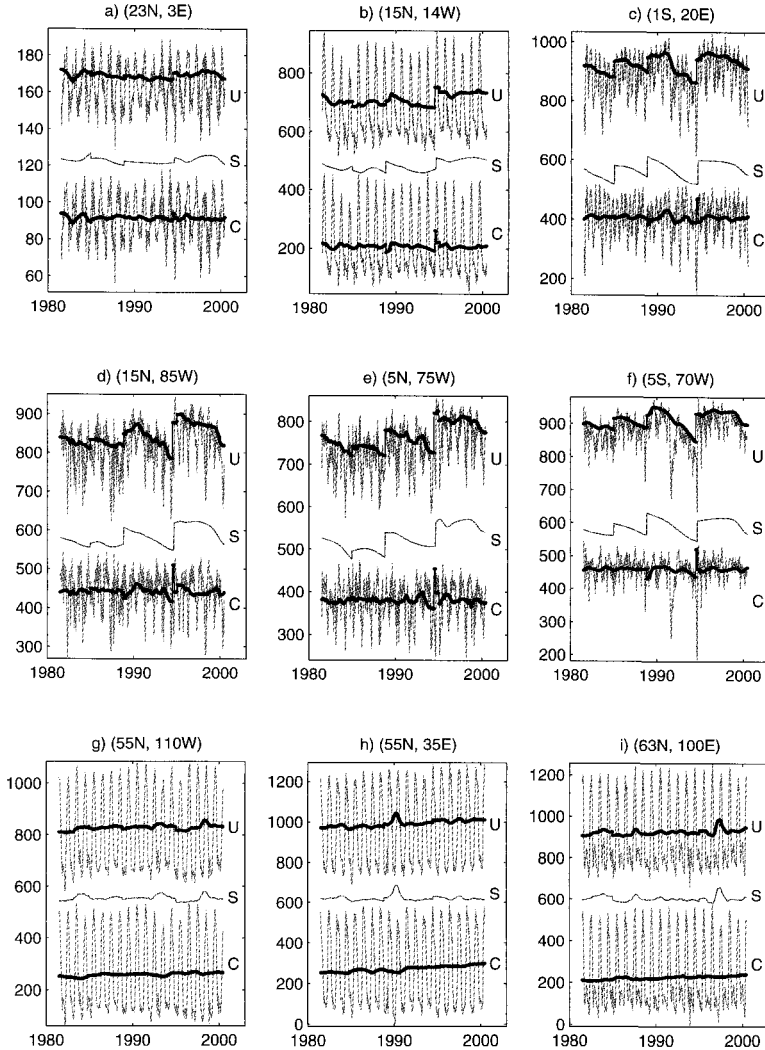


**Figure 8.4:** Each panel shows the  $NDVI \times 1000$  at different stages of the EMD-filtering scheme: the uncorrected  $NDVI$  and its associated trend ( $U$ -time series), the EMD-filtered component  $t_{szac}$  ( $S$ -time series) and the reconstructed  $NDVI$  and its associated corrected trend ( $C$ -time series) at different  $3^\circ$  by  $3^\circ$  latitude-longitude regions.  $U$ - and  $S$ -time series are shifted by the range of variation of the particular  $C$ -time series of each panel. Note that vertical scales are a function of land cover. In panel (g), the drop in 1991 is due to Pinatubo effects.

forests where the  $NDVI$  signal was shown to be most affected. Notice in Fig. 8.4 that the SZA EMD-filtering keeps the known salient features found with the  $NDVI$  time series, like the drop in the Sahel in 1984–1985 (b) due to a serious drought (Nicholson et al. 1998); the aforementioned long-term stability of deserts (a), and most tropical forests (c–f) (Los 1998); and Mt. Pinatubo’s volcanic eruption’s effects

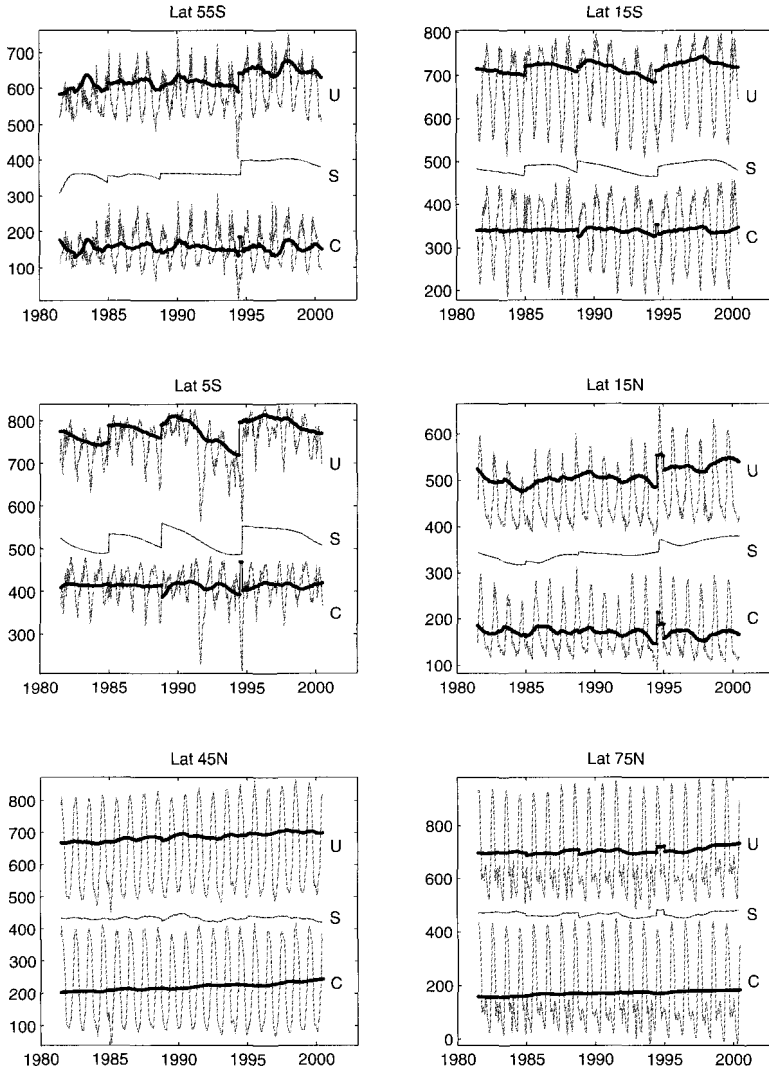


**Figure 8.5:** Each panel shows different stages of the EMD-filtering scheme, as in Fig. 8.4, of the average of  $NDVI \times 1000$  at  $10^\circ$  latitude bins. As before, the U- and S-time series are shifted by the range of variation of the particular corrected  $NDVI$  of each panel.

on high-vegetated tropical areas (f). Furthermore, an increasing trend is observed in the northern latitude panels (g–h). The corrected trends still reveal an expected discontinuity around September of 1994. This discontinuity is due to the loss of NOAA-11 and the lack of new satellites that could take its place and continue the collection of data. The only option available to preserve the continuity of the time series was the old NOAA-9 now passing over the equator in the descending node. In late January of 1995, NOAA-14 was operational and took NOAA-9's place. Lotsch

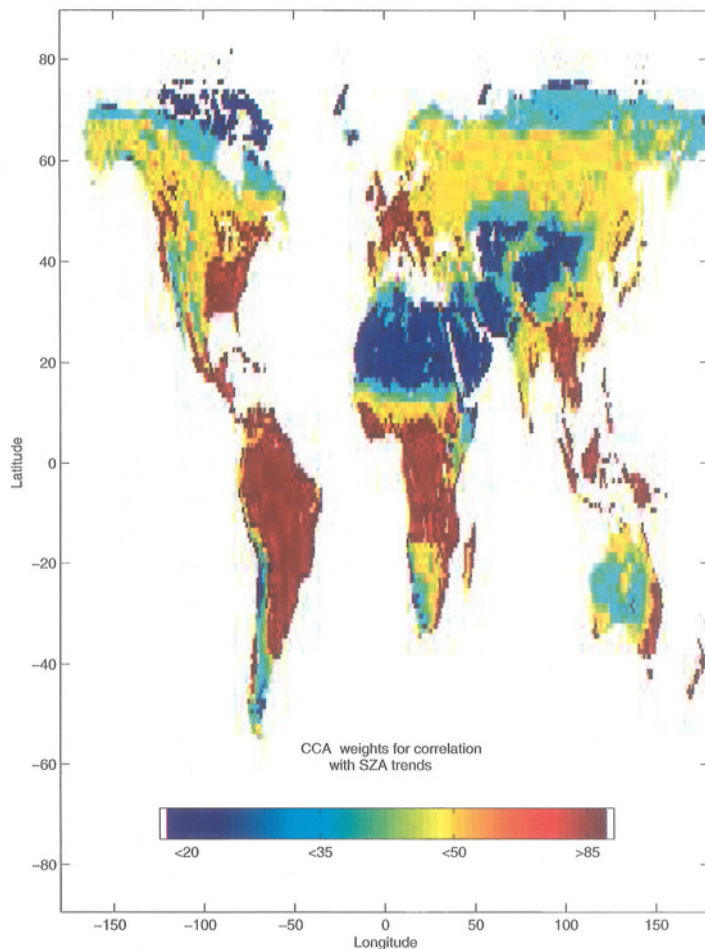
et al. (2003), applying independent component analysis (ICA) on the seasonal NDVI anomalies of the corrected data (i.e., the seasonal cycle was removed from the data before performing temporal and spatial ICA), showed that the time series is a consistent record suitable for studying long-term vegetation dynamics (Lotsch et al. 2003).

Figure 8.5 shows similar time series as in Fig. 8.4 but with  $10^\circ$  latitude bands. Although the mixture of biomes by latitude is high, these results reinforce the conclusions of Fig. 8.4 and Table 8.1, and show explicitly (LAT75N) the terminator effects upon the *NDVI* at a high solar zenith angle during winter. These results also show that the corrected trend presents a steady increase at latitudes higher than  $35^\circ$ , extending previous studies that reported only northern latitude greening for latitudes higher than  $45^\circ$  (Myneni et al. 1997, Slayback et al. 2003, Tucker et al. 2001). A thorough analysis of these trends is not within the scope of this present chapter, but should provide the quantitative confirmation of the plant growth associated with a longer active growing season at those latitudes, a confirmation that is lacking in previous studies.

Figure 8.6 shows the contribution of drift interference with the surface signal and their spatial distribution according to the canonical correlation analysis. The EMD-filtering removes *NDVI* trends that are more than 80% (red areas) correlated to the SZA trends. Areas with trends that have a lower correlation and their contribution lower than the *NDVI* uncertainty (usually less than 50%, yellow areas) were not altered. In summary, the results show that (1) regions in the tropics are the most SZA-affected due to their SZA trend magnitudes, and that (2) the high northern latitudes and regions with low vegetation biomass are less contaminated since the SZA component represents a small part of the *NDVI* signal.

## 8.6. Extension to 8-km data

Since  $1^\circ$  datasets are smoother than 8-km data due to spatial averaging, the extension of the approach to 8-km data was straightforward with a pre-processing step of a two-month temporal median nonlinear low-pass filter applied to each pixel and a krigging interpolation for missing values, especially in winter months in northern latitudes. This step increases the signal-to-noise ratio of the 8-km *NDVI* time series, allowing for the use of the time-space EMD-filtering technique without affecting trends. We applied the time-space EMD-filtering to those 8-km *NDVI* pixels whose corresponding  $1^\circ$  *NDVI*-trend has a contribution of more than 50% from the SZA trends. This contribution was quantified by applying a canonical correlation analysis between *NDVI* trends and latitudinal SZA trends (Fig. 8.6). Notably, as in the  $1^\circ$  case, there are 8-km *NDVI* pixels with large or small solar zenith angle interference. Figure 8.7 shows both cases: trend removal from the *NDVI* signal due to high correlation with the satellite drift, and trends that have not been altered because of low contribution to the *NDVI* signal from the satellite drift.



**Figure 8.6:** Contribution of drift interference with the surface signals and their spatial distribution according to the canonical correlation analysis. Red areas represent regions where the orbital drift affected the NDVI signal and the EMD correction was applied; yellow areas have a low correlation between the drift and NDVI trends and its contribution is lower than NDVI uncertainty; and blue areas are regions where calibration already accounts for possible drift artifacts.

### 8.7. Integration of NOAA-16 data

Figure 8.8 shows two EMD features that are very useful in classification problems. The NDVI seasonal variability of the Sahel is characterized by the standard deviation of the EMD-wave seasonal component. A simple classification based on uniform quantization of the median value of the EMD-trend component provides the amount of vegetation biomass expected in the region. While the classification shows the different characteristic latitudinal gradients observed in the Sahel (Nicholson et al. 1998), the standard deviation of the seasonal component identifies regions with low to high phenologic activity.

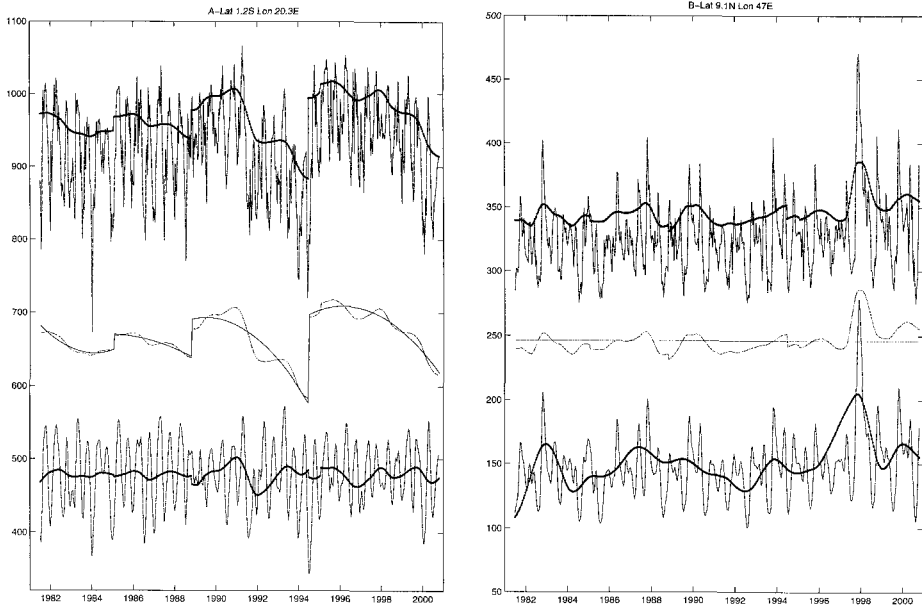


**Figure 8.7:** EMD decomposition and removal of SZA-correlated trends. (a) Tropical forest signal before satellite drift correction (series at top), trend removed (middle) and resulting series (bottom). (b) Low vegetated signal that is not corrected due to low correlation with the SZA trends. The uncorrected and trend signals are shifted by the range of variation of the particular corrected  $\text{NDVI} \times 1000$ . Note that the vertical scales are a function of land cover.

For purposes of comparison and validation, we have added a small box to the median value image that corresponds to the  $1^\circ$  box, labeled as (b), used in Figs. 8.1 and 8.4 and Table 8.1. According to the classification image, the average of the trend on this box is around 200, which coincides with the average value at  $1^\circ$  resolution (Fig. 8.4b).

These features appear as invariants and were thoroughly exploited as a result of crossovers with other satellites carrying more recent sensors. This method provides a way to account for spectral differences and, thus, to obtain significant improvements in the NDVI-AVHRR. This procedure is used as an intercalibration of the single-gain sensors aboard NOAA-7-14 (historical data) satellites and the dual-gain sensors aboard NOAA-16-17 satellites with data from SPOT-Vegetation global data. SPOT data were averaged from 1-km to 8-km globally and then decomposed by using the EMD method. The interannual EMD-trend of NDVI-SPOT signals were computed from 40 months of data, 20 months overlapping with NOAA-14 and 20 months with NOAA-16. This trend was determined to be invariant through time over the period examined. A similar trend was extracted from the same period of NOAA-14 and NOAA-16. A non-linear regression using seasonal variability and the median trend from each sensor was performed to establish the coefficients that transform the historical AVHRR record into the range of variation of the current and upcoming

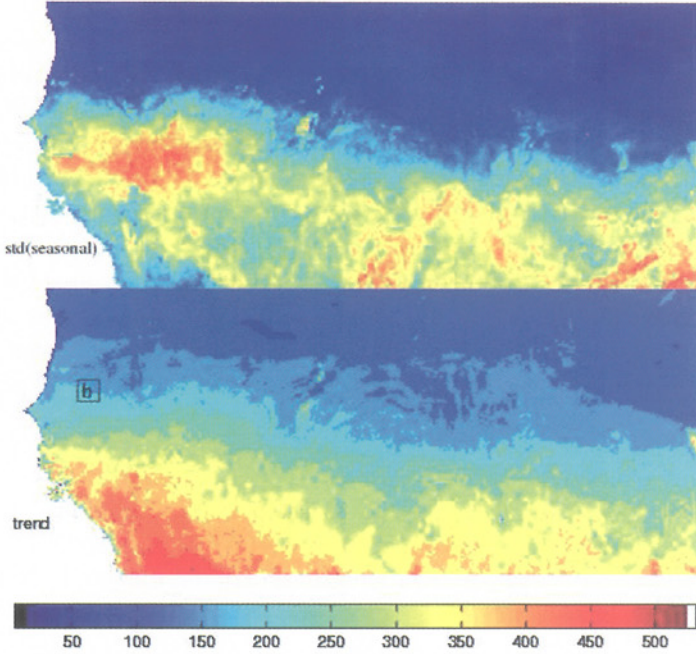


**Figure 8.8:** (a) Seasonal *NDVI* variability and classification by uniform quantization of the *NDVI* trend in the Sahel. The labeled box (b) represents the  $1^\circ$  box of Figs. 8.1b and 8.4b with a quantized median value close to 200.

suite of visible and NIR sensors, such as MODIS, SPOT-Vegetation and others. A similar procedure was performed for the NOAA-16 data. Once the trends from the historical and NOAA-16 data were transformed into the common range, the data were reconstructed, and a consistent time series was established. A krigging interpolation was applied on the integrated data to reduce noise and attenuate the effect of cloudy and missing pixels. This data will be available via ftp from the Global Land Cover Facility at the University of Maryland (available online at [www.glc.f.umd.edu](http://www.glc.f.umd.edu)).

## 8.8. Conclusions

We have presented an EMD approach for improving the *NDVI*-AVHRR time series by removing spurious SZA trends induced by satellite drift and for intercalibrating the *NDVI*-AVHRR and *NDVI* from sensors with narrow spectral bands. By using this decomposition, we found a mean trend in the *NDVI* that can be explained almost entirely by SZA trends. The remaining IMF components of the *NDVI* were found to be statistically independent of the SZA. Although the correction eliminates up to 30 percent of the variability in *NDVI* signals, it keeps all known vegetation features captured by the *NDVI* time series. Therefore, we have shown that the EMD-filtering approach for obtaining the associated mean SZA trend from

the *NDVI* time series constituted a sound *SZA* correction technique. In particular, we have removed *SZA* trends from tropical areas, especially forests, where the *NDVI* signal was shown to be more affected. As an additional gain, we have shown that the corrected *NDVI* and associated *IMFs* features can be used in concert for better spatial characterization and time series analysis. However, a thorough comparison with other measurements should be conducted in order to independently validate these results. Fortunately, in a few years time, the data archive from the new generation of satellites (*SeaWIFS*, *MODIS*, *SPOT VEGETATION*) may be long enough to allow the useful comparisons with current orbiting *AVHRR* sensors aboard *NOAA-16* and *NOAA-17*. A comparison of *ENSO*-related interannual variations in land-surface *NDVI* from *SeaWIFS* and *AVHRR* over a 2-year period does show a high degree of consistency (Behrenfeld et al. 2001).

## References

- Behrenfeld, M. J., J.T. Randerson, C. R. McClain, G. C. Feldman, S. O. Los, C. J. Tucker, P. G. Falkowski, C. B. Field, R. Frouin, W. E. Esaias, D. D. Kolber, and N. H. Pollack, 2001: Biospheric primary production during an *ENSO* transition. *Science*, **291**, 2594–2597.
- Betherton, C. S., C. Smith, and J. M. Wallace, 1992: An intercomparison of methods for finding coupled patterns in climate data. *J. Climate*, **6**, 541–560.
- Cherry, S., 1996: Singular value decomposition analysis and canonical correlation analysis. *J. Climate*, **9**, 2003–2009.
- Cihlar, J., J. M. Chen, Z. Li, F. Huang, R. Latifovic, and R. Dixon, 1998: Can interannual land surface signal be discerned in composite *AVHRR* data? *J. Geophys. Res.*, **103**, 23163–23172.
- Cihlar, J., D. Manak, and M. D'Iorio, 1994: Evaluation of compositing algorithms for *AVHRR* data over land. *IEEE Trans. Geosci. Remote Sens.*, **32**, 427–437.
- Cracknell, A. P., 1997: *The Advanced Very High Resolution Radiometer (AVHRR)*. Taylor & Francis, 300 pp.
- Cracknell, A. P., 2001: The exciting and totally unanticipated success of the *AVHRR* in applications for which it was never intended. *Adv. Space Res.*, **28**, 233–240.
- El Saleous, N. Z., E. F. Vermote, C. O. Justice, J. R. G. Townshend, C. J. Tucker, and S. N. Goward, 2000: Improvements in the global biospheric record from the Advanced Very High Resolution Radiometer (*AVHRR*). *Int. J. Remote Sens.*, **21**, 1251–1277.
- Gershenfeld, N., 1999: *The Nature of Mathematical Modeling*. Cambridge University Press, 344 pp.
- Golub, G. H., and C. F. Van Loan, 1989: *Matrix Computations*. John Hopkins University Press, 664 pp.
- Gutman, G. G., 1999: On the use of long-term global data of land reflectances and vegetation indices derived from the advanced very high resolution radiometer. *J. Geophys. Res.*, **104**, 6241–6255.

- Holben, B. N., 1986: Characteristics of maximum-value composite images from temporal AVHRR data. *Int. J. Remote Sens.*, **7**, 1417–1434.
- Huang, N.E., Z. Shen, and S. R. Long, 1999: A new view of nonlinear water waves: the Hilbert spectrum. *Annu. Rev. Fluid Mech.*, **31**, 417–457.
- Huang, N. E., Z. Shen, S. R. Long, M. C. Wu, H. H. Shih, Q. Zheng, N.-C. Yen, C. C. Tung, and H. H. Liu, 1998: The empirical mode decomposition and the Hilbert spectrum for nonlinear and non-stationary time series analysis. *Proc. R. Soc. London, Ser. A*, **454**, 903–995.
- Kaufmann, R. K., L. Zhou, Y. Knyazikhin, N. V. Shabanov, R. B. Myneni, and C. J. Tucker, 2000: Effect of orbital drift and sensor changes on the time series of AVHRR vegetation index data. *IEEE Trans. Geosci. Remote Sens.*, **38**, 2584–2597.
- Los, S., 1998: *Linkages Between Global Vegetation and Climate*. PhD thesis, Vrije Universiteit and NASA/GSFC, 179 pp.
- Los, S., C. O. Justice, and C. J. Tucker, 1994: A global 1° by 1° NDVI data set for climate studies derived from GIMMS continental NDVI data. *Int. J. Remote Sens.*, **15**, 3493–3518.
- Lotsch, A., A. F. Mark, and J. E. Pinzón, 2003: Spatio-temporal deconvolution of NDVI image sequences using independent component analysis. *IEEE Trans. Geosci. Remote Sens.*, **41**, 2938–2942.
- Mahoney, R. L., C. J. Tucker, A. Anyamba, M. Brown, D. Slayback, S. Los, J. Pinzon, J. Kendall, E. Pak, Z. Bronder, D. Grant, M. Paris, and A. Morahan, 2001: Global remote sensing of vegetation from space by the NASA/GSFC GIMMS group. *International Workshop on Global Change*, J. Kudoh and K. Yamada, eds., Sendai Kiodo Printing Co. Ltd., 17–29.
- Myneni, R. B., I. Impens, and G. Asrar, 1993: Simulation of space measurements of vegetation canopy bidirectional reflectance factors. *Remote Sens. Rev.*, **7**, 19–41.
- Myneni, R. B., C. D. Keeling, C. J. Tucker, G. Asrar, and R. R. Nemani, 1997: Increased plant growth in the northern high latitudes from 1981–1991. *Nature*, **386**, 698–702.
- Nicholson, S. E., C. J. Tucker, and M. B. Ba, 1998: Desertification, drought, and surface vegetation: An example from the west African Sahel. *Bull. Amer. Meteor. Soc.*, **79**, 815–829.
- Pinzón, J. E., J. Pierce, C. J. Tucker, and M. Brown, 2001: Evaluating coherence of natural images by smoothness membership in besov spaces, *IEEE Trans. Geosci. Remote Sens.*, **39**, 1879–1889.
- Price, J. C., 1991: Timing of NOAA afternoon passes. *Int. J. Remote Sens.*, **12**, 193–198.
- Privette, J. L., C. Fowler, G. A. Wick, D. Baldwin, and W. J. Emery, 1995: Effects of orbital drift on advanced very high resolution radiometer products: Normalized difference vegetation index and sea surface temperature. *Remote Sens. Environ.*, **53**, 164–171.

- Schaaf, C. B., F. Gao, A. H. Strahler, W. Lucht, X. Li, T. Tsang, N. Strugnell, X. Zhang, Y. Jin, J. P. Muller, P. Lewis, M. Barnsley, P. Hobson, M. Disney, G. Roberts, R. P. Dunderdale, R. P. d'Entremont, B. Hu, S. Liang, J. Privette, and D. Roy, 2002: First operational BRDF albedo and nadir reflectance products from MODIS. *Remote Sens. Environ.*, **83**, 135–148.
- Sellers, P. J., 1985: Canopy reflectance, photosynthesis and transpiration. *Int. J. Remote Sens.*, **6**, 1335–1372.
- Sellers, P. J., S. O. Los, C. J. Tucker, G. J. Collatz, C. O. Justice, D. A. Dazlich, and D. A. Randall, 1994: A global 1° by 1° NDVI data set for climate studies. Part 2: The generation of global fields of terrestrial biophysical parameters from the NDVI. *Int. J. Remote Sens.*, **15**, 3519–3545.
- Slayback, D. A., J. E. Pinzón, S. O. Los, and C. J. Tucker, 2003: Northern Hemisphere photosynthetic trends 1982–99. *Glob. Change Biol.*, **9**, 1–15.
- Trefethen, L. N., and D. Bau, 1997: *Numerical Linear Algebra*. SIAM, 361 pp.
- Tucker, C. J., 1979: Red and photographic infrared linear combinations monitoring vegetation. *Remote Sens. Environ.*, **8**, 127–150.
- Tucker, C. J., 1996: History of the use of AVHRR data for land applications. *Advances in the Use of NOAA AVHRR Data for Land Applications*, G. D'Souza, A. S. Belward, and J. P. Malingreau, eds., Brussels, 1–19.
- Tucker, C. J., D. Slayback, J. E. Pinzon, S. Los, R. B. Myneni, and M. G. Taylor, 2001: Higher northern latitude normalized difference vegetation index and growing season trends from 1982 to 1999. *Int. J. Biometeor.*, **45**, 184–190.
- Vermote, E. F., and Y. J. Kaufman, 1995: Absolute calibration of AVHRR visible and near infrared channels using ocean and cloud views, *Int. J. Remote Sens.*, **16**, 2317–2340.
- Wallace, J. M., C. Smith, and C. S. Betherton, 1992: Singular value decomposition of winter time sea surface temperature and 500-mb height anomalies. *J. Climate*, **5**, 561–576.

*Jorge E. Pinzón*

*Science Systems and Applications, Inc., Biospheric Sciences Branch, Code 614.4  
NASA/Goddard Space Flight Center, Greenbelt, Maryland 20771, USA*

*Jorge.Pinzon@ssaihq.com*

*Molly E. Brown*

*Science Systems and Applications, Inc., Biospheric Sciences Branch, Code 614.4,  
NASA/Goddard Space Flight Center, Greenbelt, Maryland 20771, USA*

*mebrown@pop900.gsfc.nasa.gov*

*Compton J. Tucker*

*Biospheric Sciences Branch, Code 614.4, NASA/Goddard Space Flight Center,  
Greenbelt, Maryland 20771, USA*

*compton@ltpmail.gsfc.nasa.gov*